Submesoscale eddies near the Kuril Straits: Asymmetric generation of clockwise and counterclockwise eddies by barotropic tidal flow

T. Nakamura,[1] J. P. Matthews,[2] T. Awaji,[2] and H. Mitsudera[1]

Received 13 November 2011; revised 23 August 2012; accepted 22 October 2012; published 12 December 2012.

[1] High spatial resolution thermal infrared (TIR) images derived by the LANDSAT Thematic Mapper (TM) sensors show the presence of numerous small-scale eddies near the Kuril Islands. As the diameters of these eddies range from around 2 to 30 km (i.e., submesoscale), they are much smaller than the eddies previously reported in this region (several tens to some hundreds of kilometers in diameter). Our simulations suggest that small-scale eddies similar to those observed in the satellite data are generated by diurnal barotropic tides. The eddy generation is well defined from Etorofu/Friza to the Onnekotan Straits, and it is caused by the effects of coastal boundaries and the stretching of water columns, which lead to eddy growth even after eddies have left the coast. We find that the counterclockwise eddies are generally larger in number and size and stronger in vorticity and surface height than the clockwise eddies in both the gradient and cyclostrophic wind balance regimes. The possible causes of such asymmetry are (1) the effect of planetary-vorticity tube stretching, which can be significant even when the final relative vorticity becomes much greater than planetary vorticity and (2) asymmetric advection by the rotating tidal flow, which advects counterclockwise eddies offshore but clockwise eddies onshore. These eddies induce strong stirring with a maximum apparent diffusivity of 10^8 cm^2 s^{-1}. The numbers, properties, and mixing effects of eddies vary greatly with the spring-neap cycle.

Citation: Nakamura, T., J. P. Matthews, T. Awaji, and H. Mitsudera (2012), Submesoscale eddies near the Kuril Straits: Asymmetric generation of clockwise and counterclockwise eddies by barotropic tidal flow, *J. Geophys. Res.*, *117*, C12014, doi:10.1029/2011JC007754.

1. Introduction

[2] The Kuril Straits are located between the Okhotsk Sea and the North Pacific Ocean (Figure 1). The transport and mixing processes taking place within the Kuril Straits are thought to play an important role in determining not only the local water mass properties but also in the ventilation of the North Pacific and in the formation of Okhotsk Seawater [e.g., *Kitani*, 1973; *Talley*, 1991, 1993; *Yasuda*, 1997; *Watanabe and Wakatsuchi*, 1998; *Nakamura et al.*, 2004, 2006a, 2006b]. Both mixing and transport are influenced by eddies, which are generated in abundance around the Kuril Straits.

[3] The eddy generation processes near the Kuril Straits, as investigated in previous studies, can be categorized into two kinds according to the horizontal length scale and the generation site of the eddies (here, eddies originating from other regions such as the Kuroshio Extension are not considered). The first type involves the generation of mesoscale eddies with diameters of around 100 km (ranging from several tens to one hundred and several tens of kilometers), and occurs widely along the Kuril Island Chain. These eddies are considered to arise mainly through baroclinic instability taking place at the density fronts that develop along the Kuril Island Chain through tidally induced vertical mixing [*Nakamura and Awaji*, 2004; *Ohshima*, 2005]. Such mesoscale eddies are generated in large numbers and are almost always present in the region, a fact which underlines their importance. An estimate based on a three dimensional tidal simulation suggested that such eddies may cause offshore water transport of 14 Sv from the Kuril Straits and have significant effects on local mixing [*Nakamura and Awaji*, 2004].

[4] The other eddy generation process leads to relatively large-scale eddies with diameters ranging from 100 to 400 km and takes place on the Pacific side of the Bussol Strait and on the Okhotsk side of the Shiretoko Peninsula, Hokkaido. The generation of these larger eddies is limited to the above two places and is thought to relate to the large inflow of Okhotsk Seawater through the Bussol Strait and to the volumes of the Soya Warm Current Water flowing through the Soya Strait, respectively [*Yasuda et al.*, 2000; *Wakatsuchi*

[1]Pan-Okhotsk Research Center, Institute of Low Temperature Science, Hokkaido University, Sapporo, Japan.
[2]Department of Geophysics, Graduate School of Science, Kyoto University, Kyoto, Japan.

Corresponding author: T. Nakamura, Pan-Okhotsk Research Center, Institute of Low Temperature Science, Hokkaido University, Sapporo, 060-0819, Japan. (nakamura@lowtem.hokudai.ac.jp)

0148-0227/12/2011JC007754

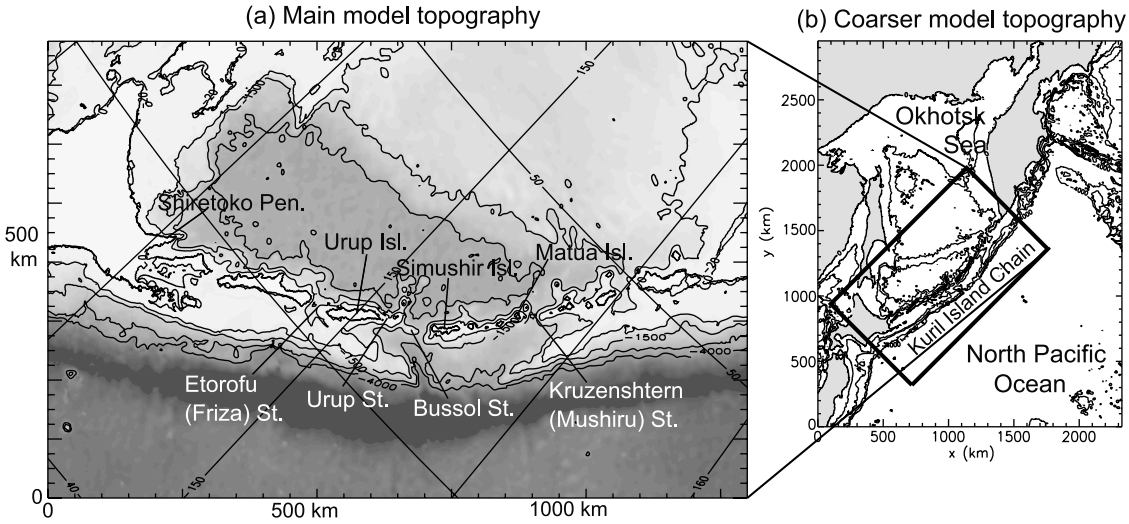

Figure 1. Model topography. (a) The main high-resolution model and (b) the coarser model. Contours are 0, 200, 500, 1500, 3000, 4000 m in Figure 1a and are 0, 500, 1500, 3000, 4000 m in Figure 1b.

and Martin, 1991; *Nakamura et al.*, 2003; *Uchimoto et al.*, 2007].

[5] In this paper, we report the discovery of eddies with much smaller horizontal scales (with diameters of 2 to ~30 km), which have been observed in high spatial resolution satellite imagery. As these small-scale eddies are numerous in and around the Kuril Straits, they may play a significant role in mixing and transport of water. Our aim is to describe the manner in which small-scale eddies are generated by diurnal barotropic tides, using a barotropic tide model. As a result, we uncovered a significant asymmetry in the generation of clockwise (CW) and counterclockwise (CCW) eddies. Cyclone/anticyclone asymmetry has been extensively studied for geostrophic turbulence [e.g., *Polvani et al.*, 1994; *Moisy et al.*, 2011], steady circulation [e.g., *Nøst et al.*, 2008; *LaCasce et al.*, 2008], or ageostrophic baroclinic instability [e.g., *Eldevik and Dysthe*, 2002]. In the present simulation, the CW/CCW asymmetry is found even in the regime of the 'cyclostrophic wind balance'.

[6] The paper is organized as follows. The observed small-scale eddies are presented in section 2 and the numerical model used is described in section 3. Results from a barotropic tidal simulation for the K_1 tide are shown in section 4, where the main properties of simulated eddies, their generation process, and the effects on mixing and transport are investigated. The effects of tidal modulation due to the K_1 and O_1 tides on the generation of eddies is investigated in section 5. The results are summarized and discussed in section 6.

2. Observed Small-Scale Eddies

[7] We have found small-scale eddies around the Kuril Islands, using high spatial resolution (approximately 90 m pixel size) LANDSAT Thematic Mapper (TM) thermal infra-red (TIR) imagery. This was done by visual inspection, considering whether the sea surface temperature (SST) anomaly has a circular shape or a spiral structure and whether it has a streamer-like feature. Examples are shown in Figure 2. CCW eddies were found to the west of Simushir Island (Figure 2a), in the western part of the Bussol Strait (Figure 2b), in the Etorofu (Friz) Strait (Figure 2d), and around Urup Island (Figure 2e), while a CW eddy was found to the southwest of the Urup Strait (Figures 2c and 2e). The diameter of the observed eddies ranged from a few kilometers to around 30 km, implying that these features are significantly smaller than those investigated in previous studies; this difference is probably attributable to their generation mechanism. Secondly, the number of CCW eddies is larger than that of CW eddies in the data we have studied so far. Thirdly, there are sites where small-scale eddies are often generated (e.g., the Etorofu Strait and southwest of the Urup Strait), where the presence of local forcing or bathymetric change is important.

[8] It should be noted that although the above examples are concentrated around Urup Island, small-scale eddies were also found in other places, particularly in the northeastern part of the Kuril Island Chain. However, in that region, strong horizontal mixing makes the observation of small-scale eddies using TIR imagery more difficult, as will be shown in section 4.7. There is a possibility that CW eddies are more likely to be overlooked if they have weaker SST signatures, and vice versa. The possibility of such asymmetry in an SST anomaly would be low in the present case, as long as the above circular or spiral shapes of SST signatures are caused by advection associated with eddies.

[9] In addition to eddies, Figure 2c exhibits anomalously cold water in and adjacent to the Urup Strait. The cold water is likely produced by vertical mixing over the sill in the Urup Strait due to tides, as suggested by modeling studies [*Nakamura et al.*, 2000a; *Nakamura and Awaji*, 2004]. Both the presence of these cold water masses and the temperature contrast between the Okhotsk Sea and the North Pacific make it easier to detect eddies in the TIR imagery.

3. Barotropic Tide Model

3.1. Equations and Parameters

[10] Numerical simulations were conducted using the barotropic tidal model of *Nakamura et al.* [2000b, hereinafter NA00].

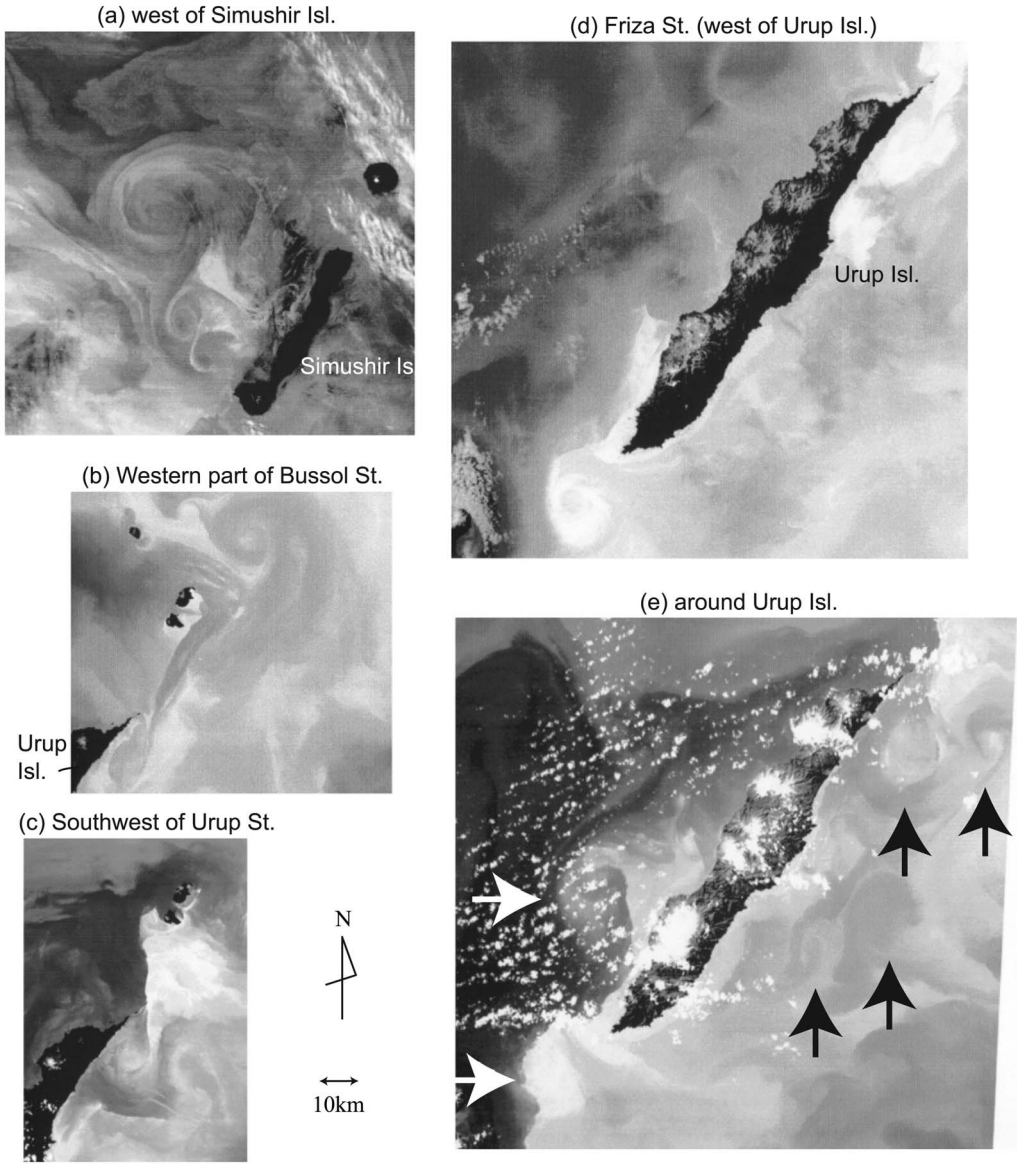

Figure 2. Small-scale eddies captured in satellite infra-red imagery (LANDSAT TM CH6). (a) West of Simushir Island (03 Jun. 1987), (b) Western part of the Bussol Strait (13 Aug. 1984), (c) Southwest of Urup Strait (18 Sep. 1991), (d) in the Etorofu (Friza) Strait (16 Aug. 1994), and (e) around Urup Island (16 Oct. 1987). Sea surface temperature is higher in darker areas and lower in lighter areas. Aligned small white patches in Figure 2e are clouds.

The governing equations of the barotropic tide model are

$$\frac{\partial \mathbf{u}}{\partial t} + \mathbf{u} \cdot \nabla_h \mathbf{u} + f\mathbf{k} \times \mathbf{u} = -g\nabla_h(\alpha_0\eta - \beta_0\zeta) - \frac{\kappa \mathbf{u}|\mathbf{u}|}{H+\eta} + A_H\nabla_h^2\mathbf{u} - B_H\nabla_h^4\mathbf{u}, \quad (1)$$

$$\frac{\partial \eta}{\partial t} + \nabla_h \cdot [(H+\eta)\mathbf{u}] = 0. \quad (2)$$

where $\mathbf{u}$ is the horizontal velocity vector, η is the surface elevation, ζ is the equilibrium tide described below, ∇_h is the horizontal component of ∇, H is the depth, $f = 2\Omega \sin\phi$ is the Coriolis parameter, g is the gravity acceleration, κ is the bottom friction coefficient, and A_H and B_H are the Laplacian and bi-harmonic horizontal eddy viscosity coefficients, respectively. The parameters α_0 and β_0 account for the effect of the tidal potential, Earth tide, and loading tide. Here we set $\alpha_0 = 0.940$, $\beta_0 = 0.736$ following *Kantha* [1995]. The equilibrium tide ζ is expressed as $\zeta = K \sin 2\phi \cos(\sigma t + \lambda)$ for diurnal tides, where K and σ are the amplitude and frequency taken from *Schwiderski* [1980], and λ and ϕ are longitude and latitude, respectively.

[11] The advection scheme in this model conserves both mass and enstrophy in addition to kinetic energy, as recommended by *Huthnance* [1981], in order to prevent spurious contributions to the torque balance, which determines the residual current strength. Note that kinetic energy is conserved only in the advection terms, but not in the

model, which has bottom drag and horizontal viscosity. In addition, although nonlinear instability is reduced by the use of an advection scheme that conserves both kinetic energy and enstrophy, grid-scale noise is generated, for example, through the presence of islands. We thus introduced biharmonic viscosity in order to reduce grid-scale noise, but this should not affect disturbances with horizontal scales of a few kilometers or more.

[12] The bottom stress is added via a quadratic law with $\kappa = 0.0026$. This formulation enables the bottom stress to generate relative vorticity around the straits, but the effects are much smaller than the stretching/squeezing effect in most straits (section 4.5.1). The horizontal eddy viscosity coefficient A_H depends linearly on the horizontal and vertical length scale as $A_H(x, y) = a_h \cdot \Delta L \cdot H(x, y)$, where ΔL is the grid length (constant in this model) and a_h is the reduced eddy coefficient [*Schwiderski*, 1980]. The value of a_h is determined to be 7.5×10^{-6} (s^{-1}) but the maximum and minimum values of A_H are set to be 10^8 cm^2 s^{-1} and 5×10^4 cm^2 s^{-1}, respectively. The coefficient for bi-harmonic eddy viscosity is set as 2×10^5 ΔL. Although the parameterization of α_0 is adopted to improve large-scale tidal elevations, it was originally designed for low-resolution global tide models; α_0 could give an artificial influence on small-scale eddies. Nevertheless, the value of α_0 is close to unity (0.94), so it hardly yields a qualitative difference.

[13] A no-slip condition is imposed at the land boundaries. At open boundaries, Orlanski's radiation condition [*Orlanski*, 1976] for velocity is used together with the sponge zone condition within 20 grids from the open boundaries where A_H increases linearly, in order to reduce artificial disturbances at the boundaries due to reflection.

3.2. Domain and Setting

[14] The domain of our main model covers the whole Kuril Island Chain (Figure 1a). The x and y axes are rotated by 45 degrees and the domain is nested into a coarser model, which includes the whole Okhotsk Sea and the surrounding regions (Figure 1b).

[15] The grid sizes are approximately 560 m in the main model and 2.4 km in the coarser model. The former grid size is more than nine times finer than the grid sizes employed in previous modeling studies on barotropic tides in the Okhotsk Sea [e.g., *Kowalik and Polyakov*, 1998; *Matsumoto et al.*, 2000; NA00]. The model topography is based on both *Smith and Sandwell* [1997] and ETOPO5 [*National Geophysical Data Center*, 1988], which are combined iteratively depending on the magnitude of discrepancies. After data are combined, the model depths are similar to ETOPO5 depths in relatively large scales (averages over about $1° \times 1°$), whereas fine structures are maintained, though their amplitudes are reduced depending on discrepancies from ETOPO5 (larger reduction for larger discrepancies). As a result, abnormal values detectable by visual inspection are corrected (Figure 1). Because our aim is not to achieve an improvement in prediction accuracy of tides, we consider the remaining discrepancies from the true bathymetry to be permissible for the sake of at least a qualitative argument.

[16] For the main forcing, tidal elevation is specified at open boundaries using the results of *Matsumoto et al.* [2000] as input for the coarser model, and these results are in turn used for the main model. Thus, both models are forced by the boundary oscillations in addition to the effects of the tide generating potential, the Earth tide, and the ocean loading tide, which are given at all grid points.

[17] In this study, we focused on the K_1 tide, as the largest tidal constituent in current speed around the Kuril Straits. In addition, the influence of tidal modulation associated with the K_1 and O_1 tides was investigated based on three numerical experiments. In two of these experiments the K_1 and O_1 tides were calculated separately, and in the third experiment the two tidal constituents were calculated simultaneously (K_1, O_1, and $K_1 + O_1$ cases, respectively). The initial conditions were zero currents and a flat sea-surface and the integrations were done for 40 days in the K_1 and O_1 cases and for 50 days in the $K_1 + O_1$ case.

[18] Large scale features in the calculated elevation field of the K_1 tide are basically the same as those of NA00 (not shown for conciseness) and are similar to the results of data assimilation and satellite observations [e.g., *Matsumoto et al.*, 2000; *Ray*, 1999]. In fact, a comparison with the International Hydrographic Office tidal harmonic constants yields correlation coefficients between the calculated and the observed harmonic constants of 0.7 for phase and 0.8 for amplitude for the K_1 tide (the sites used are shown in NA00). Also, the root mean square misfit of elevation calculated in the manner shown in NA00 is 6.3 cm. The results for the O_1 tide are also qualitatively similar to the observations. Given the similarity in the large-scale elevation field, we consider that the qualitative features of the current field are reasonably well reproduced.

4. Eddies Generated by the K_1 Barotropic Tide

4.1. Background Tidal Currents and Mean Flow

[19] The flow field induced by the K_1 tide (inclusive of the temporal average and higher frequency components) during a tidal cycle is shown in Figure 3, for the central area of the Kuril Straits where eddies are actively generated.

[20] Qualitatively, features with relatively large spatial scales are similar to those found in NA00. For example, currents are swift near the straits or islands due to shallow depths and contraction by side boundaries, and current vectors rotate clockwise with time in most straits. Topographically trapped waves are generated over the slopes and circulate around the islands or banks as indicated in Figure 3, in which the waves resemble propagating pulses of current. These trapped waves are important for amplifying currents around the Kuril Straits, and their presence has been confirmed from observational studies [e.g., *Rabinovich and Thomson*, 2001]. In addition, the effects of viscous barotropic waves [*Lee and Kim*, 1999] could be important around islands near Hokkaido, where the continental shelf is wide and shallow. Quantitatively, however, there are significant differences between our results and the NA00 case. Owing to the higher resolution, the structure of the trapped waves are much better resolved, and currents are swifter with a maximum speed reaching 3.1 ms^{-1}, which includes mean and eddy components.

[21] The mean flow is also qualitatively similar to that calculated by the NA00 model, as shown by the distribution of the Eulerian mean transport stream function (Figure 4). The mean currents are generally strong over slopes and tend to circulate around islands or banks with the shallower area

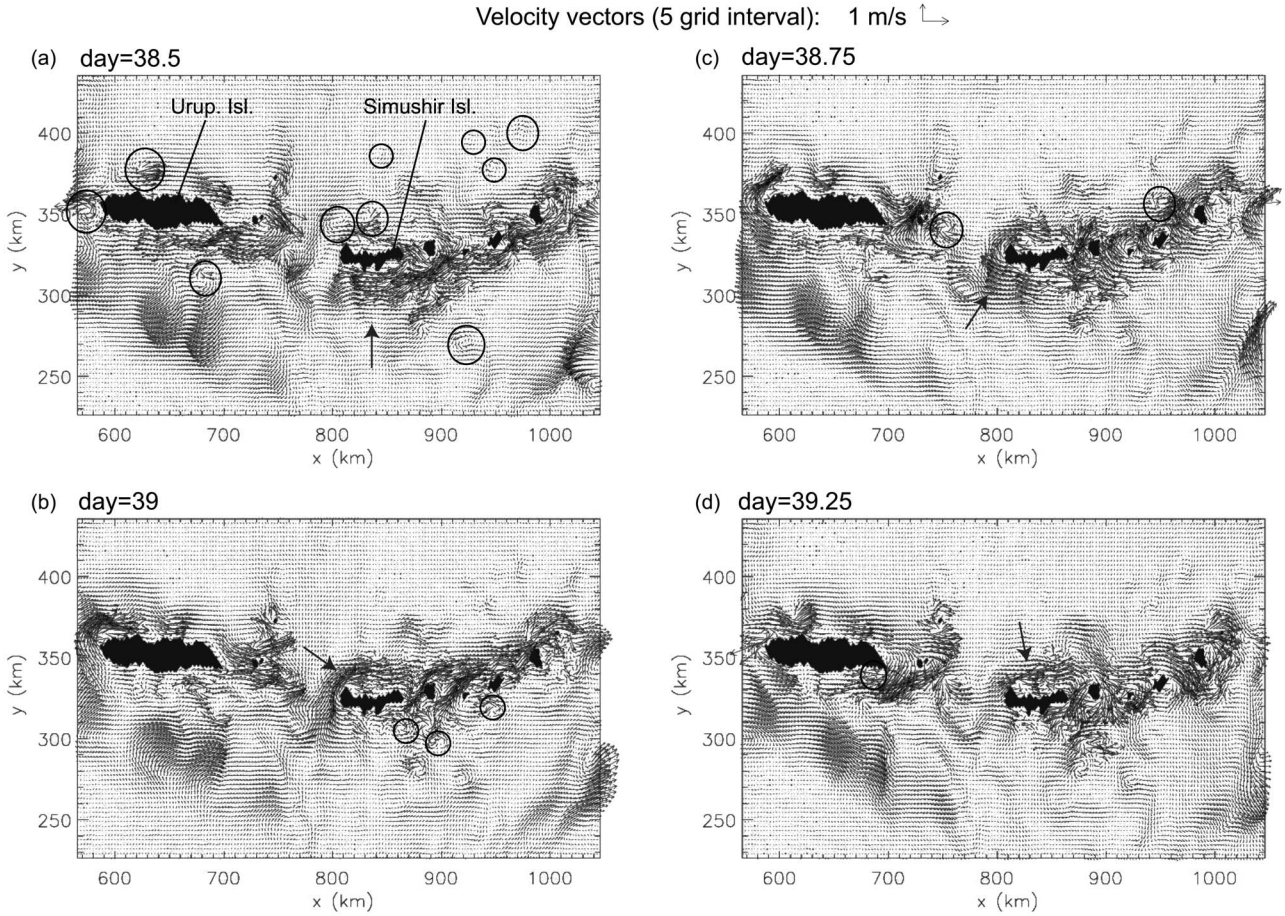

Figure 3. Velocity field during a K_1 tidal cycle around the central part of the Kuril Straits (from the Kruzenshtern to Etorofu Straits). Current vectors are plotted with 5 grid intervals in both x and y directions. Large arrows indicate examples of topographically trapped waves. Circles indicate small scale eddies, which are easily seen away from the straits in this figure due to the interval and length of current vectors.

on the right; they are formed mainly through vorticity redistribution by tidal flow advection [*Robinson*, 1981] and topographically trapped waves (NA00), although eddy-like features are still visible in the offshore regions where mean currents are weak. Quantitatively, the mean currents obtained here are generally stronger than those obtained by NA00, owing to the much higher spatial resolution, though the maximum value converges (0.7 ms^{-1} for 5 km resolution, 0.9 ms^{-1} for 2.5 km (NA00), and 0.97 ms^{-1} for 560 m). Nevertheless, the mean flow is generally weak over sill tops, and hence it affects eddy propagation after development rather than eddy generation which takes place over sill tops as shown below.

4.2. Small Scale Eddies Similar to Those Observed in Satellite TIR Data

[22] On smaller scales, numerous eddies are seen in the flow field shown in Figure 3 (though eddies near the straits are difficult to identify in Figure 3 owing to the length and interval of current vectors). Some eddies are so strong that they produce significant sea surface height (SSH) anomalies (more than 10 cm; Figure 5). Such eddy-induced SSH anomalies are strong near the straits, particularly from Simushir Island

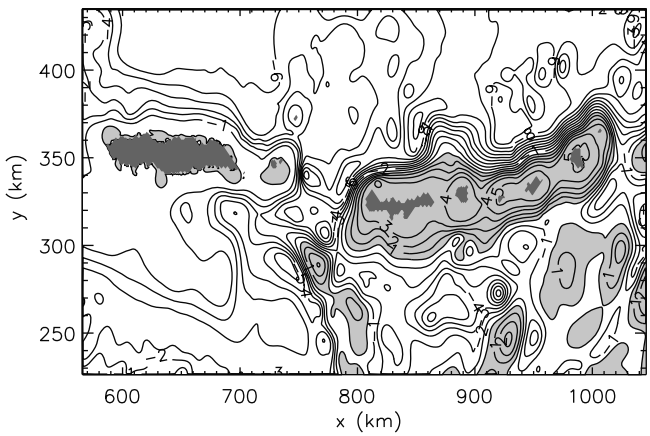

Figure 4. Eulerian time-averaged transport stream function produced by the K_1 tide. Values in shaded areas are positive. Contour interval is 1 Sv. The time duration of average is chosen as three cycles to reduce the contamination due to eddies.

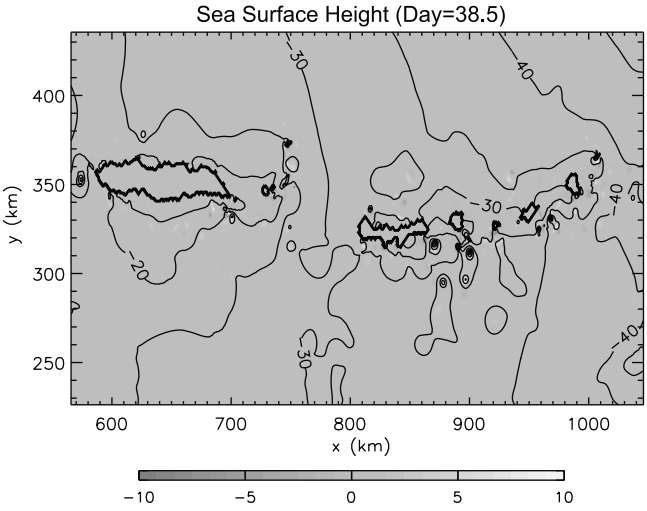

Figure 5. Same as Figure 3a, but for sea surface height (contours) and relative vorticity (tone). Contour interval is 5 cm.

to Matua Island (x = 850–1000 km). These simulated eddies have a small horizontal scale, and their diameters are of order 10 km, ranging from a few kilometers to around 30 km, values that are similar to those of the observed eddies shown in the TIR images discussed in section 2.

[23] Also, some simulated eddies are generated at or are passing close to the locations where eddies are observed in the satellite data, and are rotating in the same direction. For example, to the west of Urup Island, a CCW eddy with a diameter of approximately 15 km is produced periodically in the simulation (Figures 3a and 5). This feature resembles the observed eddy shown in Figures 2d and 2e. Also, CCW eddies to the west of Simushir Island (Figure 3a), in the western part of the Bussol Strait (Figure 3b), and to the south of Urup Island (Figures 3a and 3c) are similar to those seen in Figures 2a, 2b, and 2e, respectively. In addition, a CW eddy generated on the southwest of the Urup Strait (Figure 3d) is similar to that seen in Figure 2c, though the simulated eddy is not very clear in this figure.

[24] The observed similarities between the satellite imagery and the simulation data indicate that the barotropic tidal flow is a main cause of the observed small-scale eddies.

4.3. Eddy Generation and Propagation

[25] Figures 6 and 7 show eddy generation and propagation around the northeastern end of Simushir Island and nearby straits, where energetic eddies are produced in the model. When the tidal flow is directed toward the Okhotsk Sea (Figures 6a–6c), two eddies (labeled as A and B) are generated in the area of the figure. As the tidal-flow direction rotates clockwise near the straits (Figures 6c and 6d), the eddies move away due mainly to advection, and are also affected by the bottom topography and other effects. These eddies grow so strong that their relative vorticity becomes more than ten times greater than the local planetary vorticity (i.e., f) at maximum. When the tidal flow is directed toward the Pacific, an eddy labeled C is similarly generated and this then moves away (Figures 7a–7d).

[26] A closer look reveals that these eddies are generated on the downstream side of the islands (or 'headland'). For example, eddy A is generated adjacent to Simushir Island on the Okhotsk side when the tidal flow is directed to the Okhotsk Sea (Figure 6a). This is a characteristic feature of the so-called headland eddy and indicates the importance of vorticity supply from the coast due to lateral friction and/or of the shape of coastal geometry in the generation of the eddies [e.g., *Signell and Geyer*, 1991; *Klinger*, 1994]. In fact, anomalous vorticity extends offshore from the coasts to the eddies (e.g., Figures 6b, 6c, and 7b for eddies A, B, and C, respectively). Note that in the present case, it would be permissible to consider each side of an island separately, and one side of an island may be considered as the headland. This is because eddies generated on one side interact infrequently with those generated on the other side, or interaction takes place after eddy generation and growth.

[27] Two other characteristic features are observed here, which are not usually seen in shallow water headland eddies. First, the eddies continue growing in both vorticity and SSH anomaly, after they leave the coasts (e.g., eddy A in Figures 6b–6d). Such growth cannot be caused by the effects of coastal boundaries. This suggests the presence of another important source of vorticity, which is examined in section 4.5.1.

[28] Secondly, eddies generated on the left of straits (facing downstream) are in general much stronger and larger than those on the right, and thus most strong eddies are CCW. In contrast, the vorticity supply from coastal boundaries should occur on both sides of a strait, so that it generates eddies on both sides: a CCW eddy on the left of the strait when facing downstream and a CW eddy on the right with similar size and strength (if the coastal shape and flow are symmetric).

[29] Similar features are also seen in other straits. As another example, Figure 8 shows eddy generation in the eastern part of the Etorofu Strait. A CCW eddy generated on the left side coast facing downstream moves away from the coast and grows into a strong cyclonic eddy (Figures 8a and 8b). On the other hand, although CW eddies are generated on the right side coast facing downstream in this strait, these eddies are weaker and smaller than the CCW eddy and gradually disintegrate (Figures 8c and 8d). Consistent with the simulated eddy formation, the phases of the barotropic tidal flow at the observation times of CCW eddies in Figures 2d and 2e are close to that at the time when simulated CCW eddies are well developed (not shown).

4.4. Asymmetry in Eddy Statistics

[30] To confirm the asymmetry of CW and CCW eddies, statistical properties of eddies are estimated. Two definitions of eddies are used; one definition based on SSH and the other based on the Okubo-Weiss parameter OW [*Okubo*, 1970; *Weiss*, 1991; *Isern-Fontanet et al.*, 2006]. Two definitions are used because although SSH clearly shows strong eddies as seen in Figure 6, it would underestimate the number (and size) of anticyclones if they are in the 'gradient wind balance' regime. Thus, we also use OW, which characterizes the topology of the velocity field and is defined as $OW = s_n^2 + s_s^2 - \omega^2$, where s_n and s_s are the normal and shear components of strain, respectively, and ω is the relative vorticity.

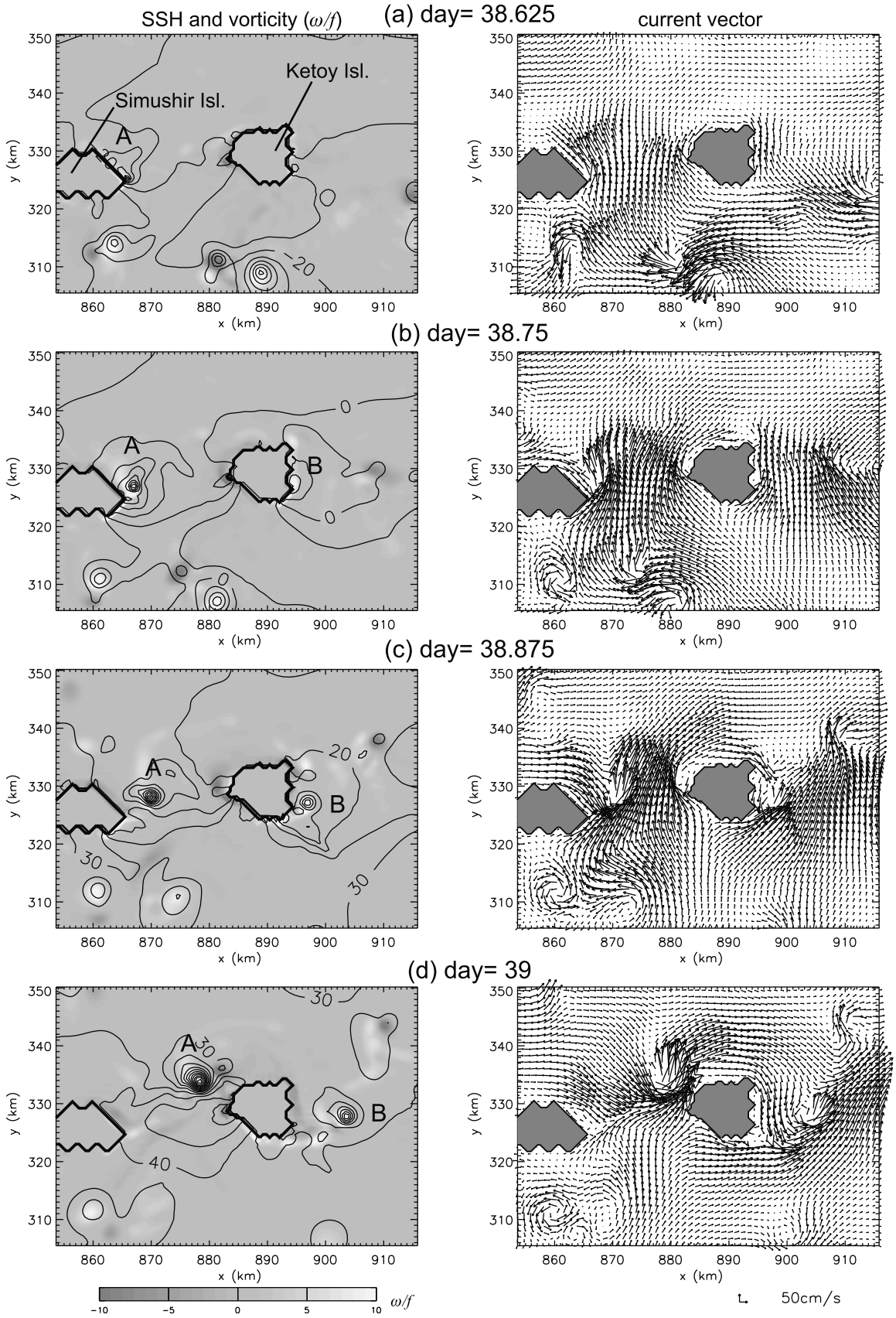

Figure 6. Time series of the distribution of (left) sea surface height (contours) and relative vorticity (tone) and (right) current vectors around the northeastern tip of Simushir Island. Contour interval is 5 cm. Current vectors are drawn at every two grids in both *x* and *y* directions.

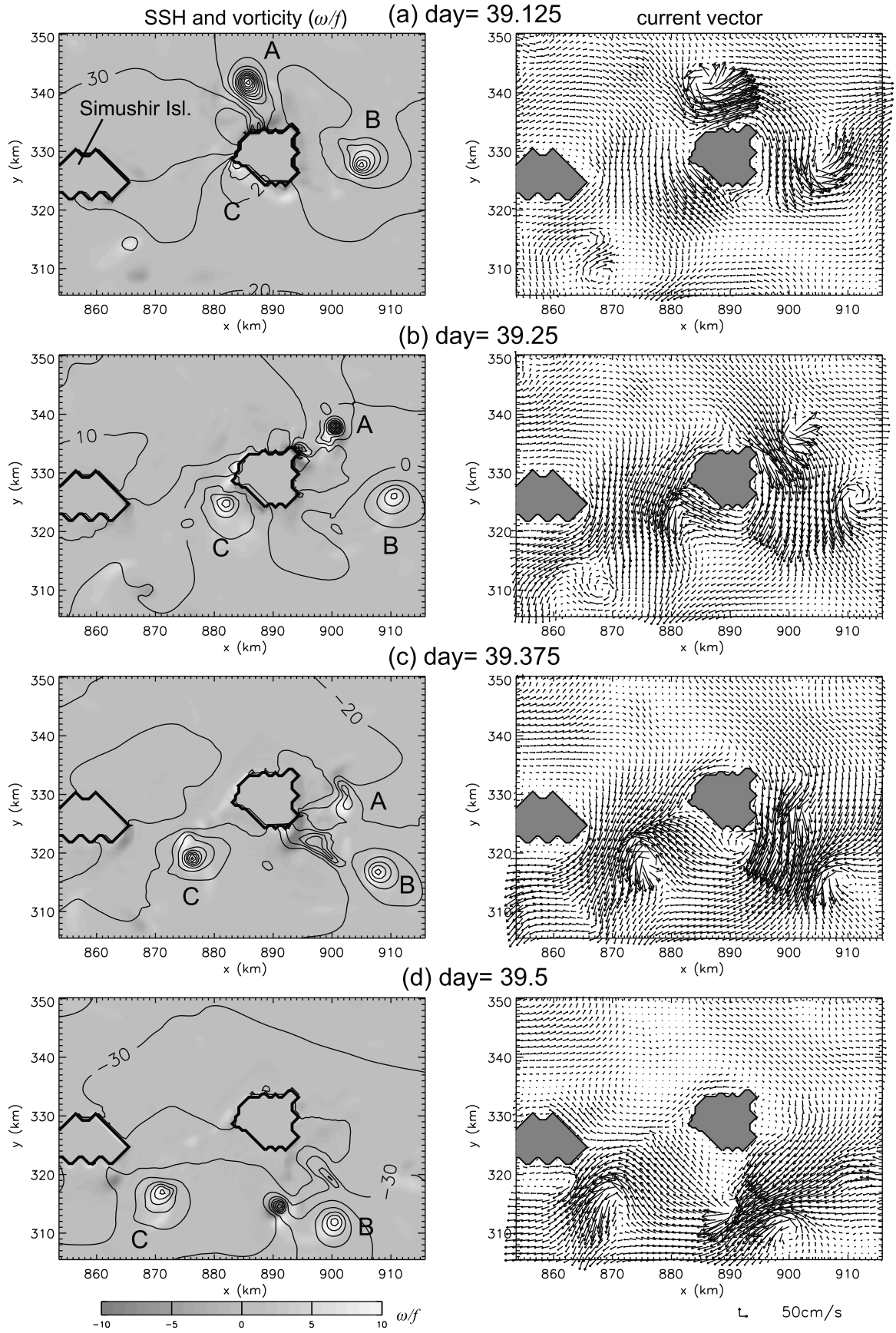

Figure 7. Same as Figure 6, but for the latter half of the tidal cycle.

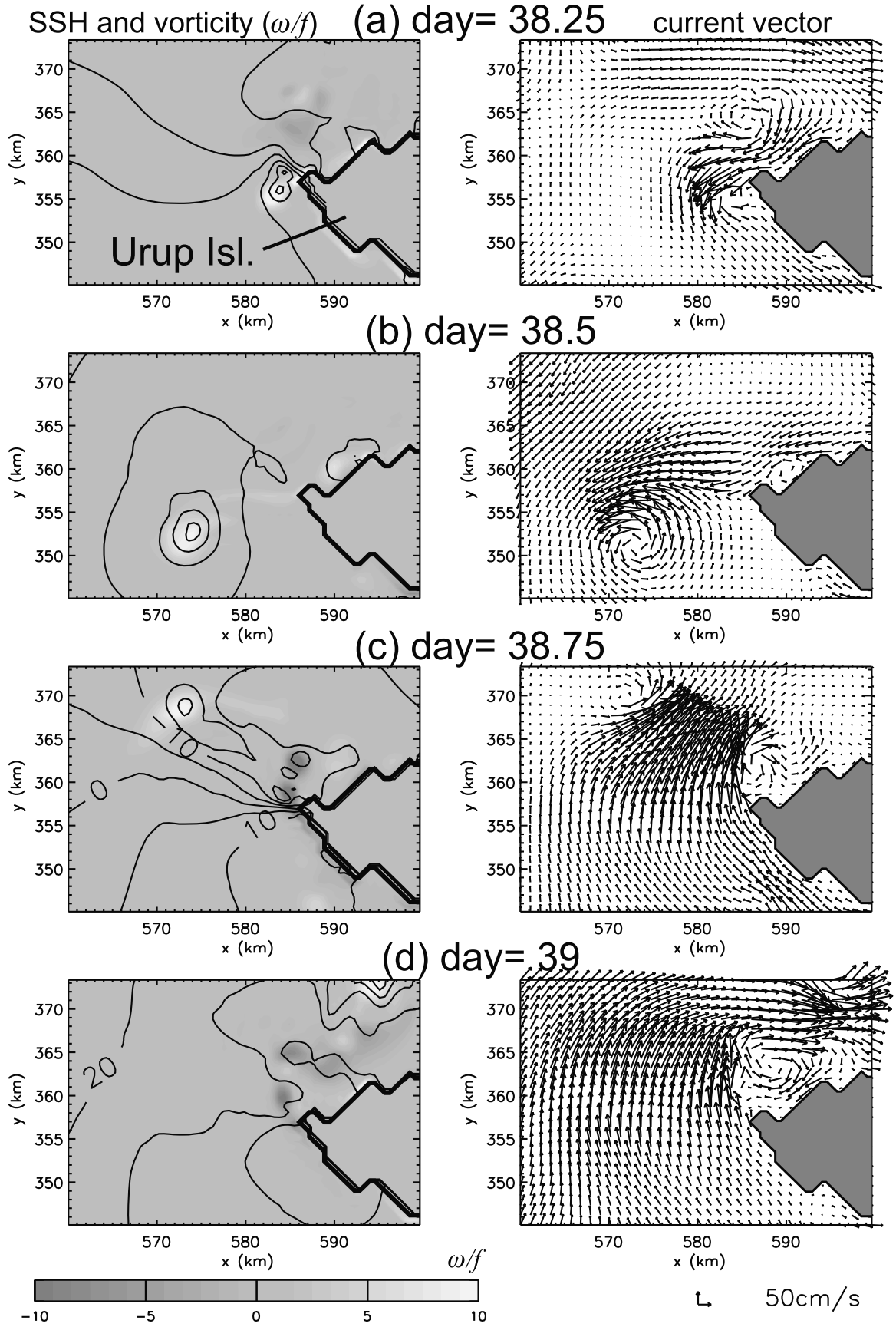

Figure 8. Same as Figure 6, but around the southwestern tip of Urup Island and with a time interval of 0.25 day.

[31] In the definition based on the SSH anomaly (η'), an eddy is defined as a connected region that satisfies the conditions: (1) $|\eta'| \geq 10$ cm for areas shallower than 500 m or $|\eta'| \geq 5$ cm for other areas and (2) the area of the region should be greater than three grids. Here, η' is calculated as the deviation from the horizontal running mean in a 45 km × 45 km area to remove large-scale tidal elevation. The larger threshold value in shallow areas is imposed to exclude SSH anomalies associated with small-scale tidal elevation such as those induced by shelf waves around islands. In the definition based on *OW*, an eddy is defined as a connected region that satisfies the conditions: (1) $OW \leq -2.5 \times 10^{-7}$, where the threshold value is 2 standard deviation of *OW*, (2) the area of the region should be greater than three grids, and (3) the distance from the land should exceeds two grids. The threshold value of *OW* is higher than values often used in open ocean applications to exclude contamination by tides and associated flow or waves. Further, regions adjacent to land are avoided to exclude contamination by land boundary effects. Changes in the threshold value of ±1 standard deviation did not result in a qualitative difference but changes in scatter.

[32] After the eddies are defined, the vorticity amplitude (ω_a), SSH amplitude (η_a), and equivalent radius (R) are calculated at every 1/24 tidal period. Here, ω_a is the maximum vorticity in a CCW eddy or the minimum vorticity for a CW eddy, η_a is defined as the difference between the maximum and minimum η' in an eddy with the sign set to be positive for convex η' and negative for concave, and R is the radius of an equivalent circular eddy with the same area.

[33] These properties are presented as scatterplots of vorticity amplitude vs SSH amplitude (Figures 9a and 9d) and equivalent radius (Figures 9b and 9e), in which eddies detected in all the 24 tidal phases are plotted. The eddy properties calculated from the definitions based on SSH and *OW* are qualitatively similar, although the SSH-based definition shows larger radius and scatter. In fact, eddies defined by the SSH anomaly roughly corresponds to those defined by *OW*, excluding relatively weak eddies. These similarities and correspondence suggest that the asymmetry discussed below is robust for eddy definitions.

[34] The above scatterplots indicate the CW/CCW asymmetry. CCW eddies tend to be larger in size and number and stronger in SSH and vorticity in the present simulation. This tendency is in contrast to geostrophic turbulence, where cyclones (CCW) tend to be smaller and more prone to elongation and breakage, whereas anticyclones (CW) tend to be larger.

[35] The force balance is in fact different from geostrophic turbulence. If we assume axial symmetry and constant vorticity (i.e., corresponding to the core of the Rankin vortex), the force balance in the radial direction yields

$$\left(\frac{\omega_c}{f}\right)^2 + 2\left(\frac{\omega_c}{f}\right) = -8\alpha_0 g \frac{\eta_a}{f^2 R^2}, \tag{3}$$

where ω_c is the vorticity assumed to be constant. The first term on the left-hand side represents the centrifugal force; the second, the Coriolis force; and the term on the right-hand side, the pressure gradient force. The scatterplots of vorticity amplitude and the term on the right-hand side are shown in Figures 9c and 9f. Eddies shown in the plots are distributed around the curve representing the left-hand side of equation (3) with the approximation $\omega_c = \omega_a$, though the scatter is large. For most of these eddies, the centrifugal force is much stronger than the Coriolis force; the value of the first term in equation (3) is more than five times that of the second term when $|\omega|/f > 10$. Indeed, no eddies in the figure have positive SSH amplitudes, which require $-2f < \omega < 0$. These facts indicate that the eddies shown in Figure 9 are in the cyclostrophic wind balance regime.

[36] Nevertheless, this does not mean that all eddies are in the cyclostrophic wind balance regime. Weak eddies, which are excluded from eddy detection, are governed by the gradient wind balance. For weak CCW eddies, typical values of radius (r), current speed in the azimuthal direction (v_a), and SSH amplitude are estimated to be around 10 km, 50 cm s^{-1}, and 10 cm, respectively. These values yield a rough balance among the pressure gradient force per unit mass ($\sim -\alpha_0 g \eta_a / r$), the Coriolis force ($f v_a$), and the centrifugal force (v_a^2/r), which are calculated to be -9×10^{-3}, 5×10^{-3}, and 2.5×10^{-3} (cm s^{-2}), respectively.

4.5. Possible Causes of the Asymmetry

[37] Previous studies have shown that asymmetry in cyclonic and anticyclonic eddies can occur because of limitations due to the gradient wind balance [cf. *Holton*, 1992] or centrifugal instability or shear instability [e.g., *Dong et al.*, 2007; *Kloosterziel and Van Heijst*, 1991; *Ooyama*, 1966], which would have some relevance for the present case. For CW anticyclonic eddies, the gradient wind balance requires the condition $0 \leq v_a \leq fr/2$ to be met. Anticyclonic eddies therefore have an upper limit in terms of both current speed and vorticity, or a lower limit in the horizontal scale. Also, asymmetry in instability could have some effects, as disintegration of a CW eddy takes place in the model (Figure 8). However, the present asymmetry of CW and CCW eddies are produced even in the regime of the cyclostrophic wind balance, and many CW eddies grow rapidly (in a few hours) without disintegration. These may suggest the presence of an alternative effect. We thus begin with an investigation of the eddy growth mechanism, based on which possible causes of asymmetry are reconsidered.

4.5.1. Vorticity Analysis

[38] To investigate the eddy growth mechanism, we have analyzed vorticity generation using the vorticity equation,

$$\frac{D\omega}{Dt} = \underbrace{-f\nabla_h \cdot \mathbf{u}}_{(a)} \underbrace{-\omega \nabla_h \cdot \mathbf{u}}_{(b)} + \underbrace{\mathbf{k} \cdot \left[\kappa \mathbf{u} \times \frac{\nabla_h |\mathbf{u}|}{H+\eta} + \kappa \mathbf{u} \times |\mathbf{u}| \nabla_h \left(\frac{1}{H+\eta}\right)\right]}_{(c)} + \text{damping terms}, \tag{4}$$

which is obtained by taking the curl of the momentum equation (1). Here, D/Dt represents the Lagrangian time variation and $\mathbf{k}$ is the unit vector in the vertical direction. The β term and other small terms arising from the spatial variation of the horizontal eddy viscosity coefficient are neglected. Terms (a) and (b) change vorticity by vortex-tube stretching or shrinking. For term (a), the generated vorticity acquires positive and negative values for stretching and shrinking, respectively, while the vorticity generated by term (b) changes sign in association with the sign of local relative

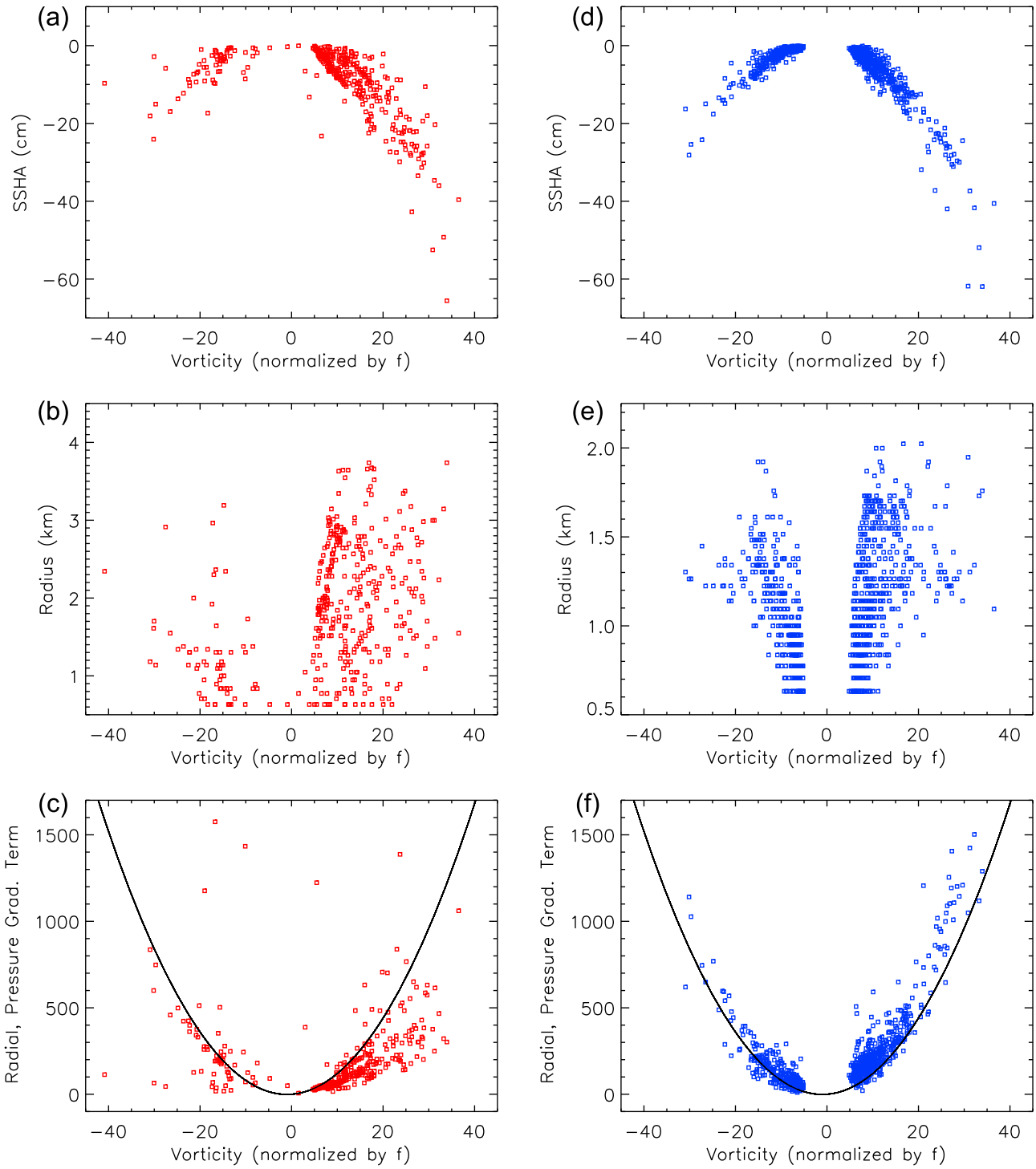

Figure 9. Statistics of eddies defined from (a–c) sea surface height (SSH) anomaly and (d–f) the Okubo-Weiss parameter. Scatterplots of vorticity amplitude (ω_a) normalized by f vs (top) SSH amplitude η_a, (middle) equivalent radius R and (bottom) the pressure gradient term $(-8\alpha g\eta_a/(fR)^2)$ estimated with assumptions of axial symmetry and constant vorticity. Under these assumptions, a theoretical line of the sum of the centrifugal and Coriolis force terms $(\omega_a/f)^2 + 2(\omega_a/f)$ is drawn in Figures 9c and 9f. Detailed definitions are described in section 4.4.

vorticity. Term (c) represents vorticity generation by bottom friction for a quadratic friction law in the presence of velocity shear and for a horizontal gradient of water depth transverse to the direction of the tidal flow [*Robinson*, 1981]. The vorticity supply due to the presence of lateral boundaries is not included in this formulation because the supply occurs through boundary conditions.

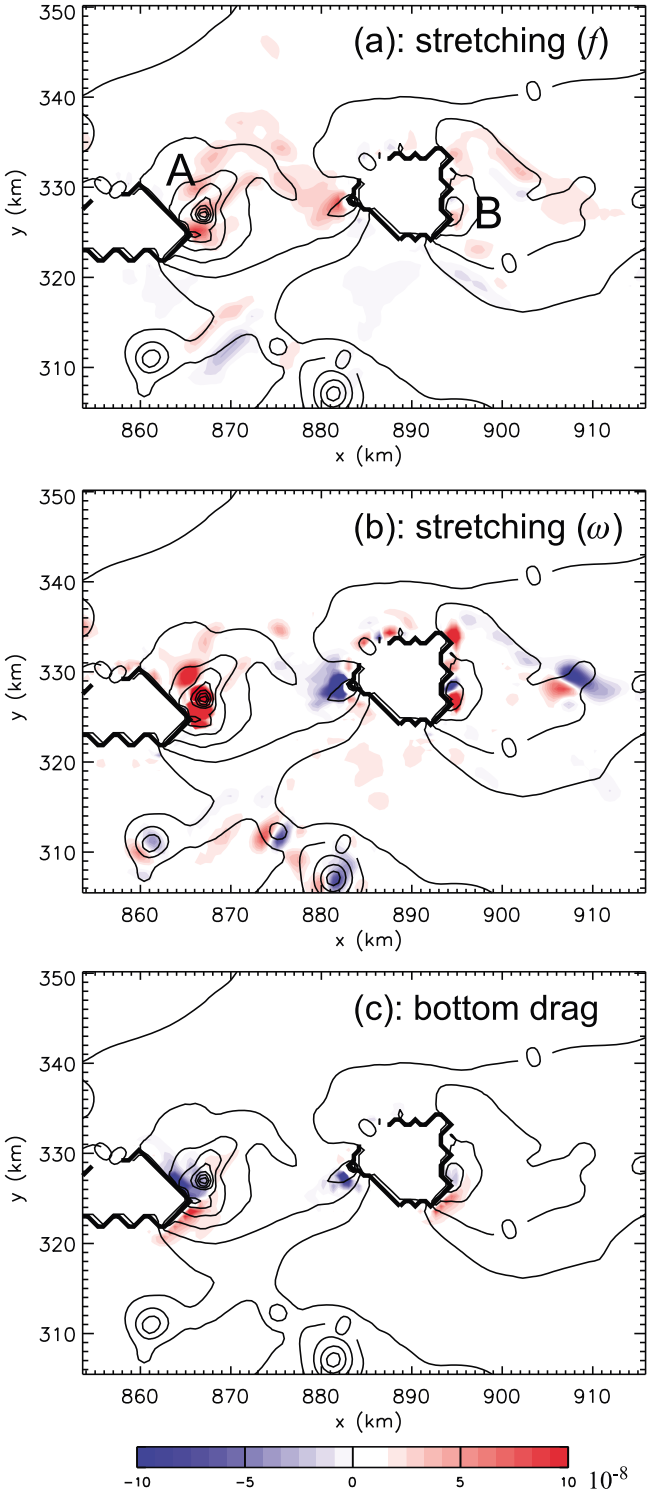

Figure 10. The distribution of vorticity generation terms defined in equation (4) at day 38.75, when the flow toward the Okhotsk Sea is strongest and generating the eddies A and B. Values in red and blue areas are greater than 10^{-9} and less than -10^{-9} s^{-2}, respectively. Contours of sea surface height are superposed.

[39] Figure 10 shows the distributions of the vorticity generation terms in equation (4), when the flow toward the Okhotsk Sea is nearly at a maximum and eddies A and B are growing (corresponding to the time of Figure 6b). The relative importance of the terms described below is essentially similar for other eddies. In and around eddies A and B, the stretching term (b) is much larger than the other two vorticity generation terms. As this term has the same sign as the vorticity of the eddies, it therefore serves to strengthen them. This occurs as the eddies are advected to the deeper region, leading to the stretching of the water column (i.e., $-\nabla_h \cdot \mathbf{u} > 0$). Accordingly, the stretching of a (relative) vorticity tube is the main cause of the growth after leaving the coast.

[40] Term (b), however, enhances both CCW and CW eddies in the stretching condition, and thus it seems an unlikely cause of asymmetry in the eddy generation process. Term (c), the effect of bottom friction, is much smaller, and tends to dissipate eddies through a mechanism similar to the Ekman spin down due to the first term in the bracket of term (c). Term (c) sometimes works to reduce the asymmetry (e.g., the bottom drag term supplies negative vorticity, weakening the CCW eddy A but strengthening the CW eddy on the other side of the strait at the time shown in Figure 10). On the other hand, term (a) can cause asymmetry as it strengthens CCW eddies and weakens CW eddies in the stretching condition; Next, we estimate the effects of planetary-vorticity tube stretching.

4.5.2. Effect of Planetary-Vorticity Tube Stretching

[41] To focus on vortex tube stretching, let us suppose the conservation of potential vorticity

$$\frac{\omega + f}{H} = \frac{\omega_0 + f}{H_0},$$

where ω_0 and H_0 are the initial vorticity and depth, respectively. In the present case, ω_0 is mainly caused by lateral friction on the coast. It then yields

$$\frac{\omega}{f} = \left(\frac{H}{H_0}\right)\left(\frac{\omega_0}{f}\right) + \left(\frac{H}{H_0}\right) - 1. \tag{5}$$

This indicates that as long as $\omega_0/f = O(1)$, f causes a significant bias in eddy growth, even if $\omega \gg f$.

[42] For a more quantitative argument, consider the ratio of ω with $\omega_0 < 0$ to ω with $\omega_0 > 0$ for the same $|\omega_0|$ and H_0 values, as it is a more useful measure of asymmetry than the difference of the two. The ratio becomes

$$\mu = \frac{\omega(\omega_0 < 0)}{\omega(\omega_0 > 0)} = \frac{-\left(\frac{H}{H_0}\right)\left(\frac{|\omega_0|}{f}\right) + \left(\frac{H}{H_0}\right) - 1}{\left(\frac{H}{H_0}\right)\left(\frac{|\omega_0|}{f}\right) + \left(\frac{H}{H_0}\right) - 1}, \tag{6}$$

and is shown in Figure 11 as a function of H/H_0 and ω_0/f. The range of the ratio μ is $[-1, 1]$, and by definition, the asymmetry strengthens as μ increases from -1, at which the growth is symmetric. (When $\mu = +1$, it represents translational symmetry geographically. This is, however, not of particular interest here.) As seen in Figure 11, μ is mostly determined by ω_0/f, if $H/H_0 \gtrsim 3$.

[43] In the present simulation, ω_0/f ranges roughly from 2 to 5 for strong eddies, and H/H_0 from 2 to 10 during the rapid growth of eddies. These parameter ranges yield the ratio μ of $-1/3$ to $-2/3$, suggesting the presence of significant

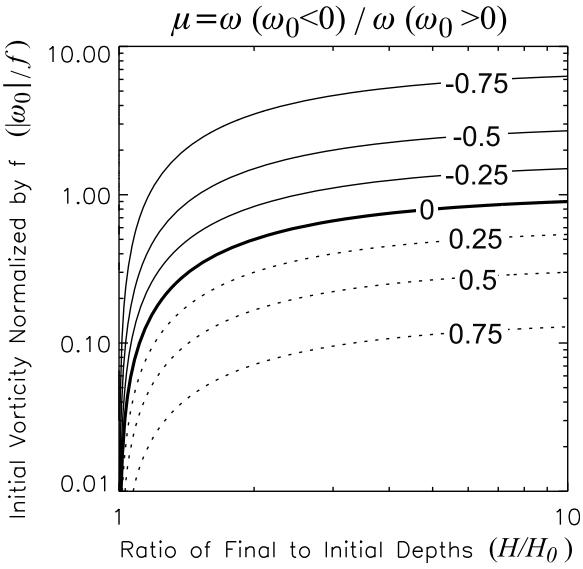

Figure 11. Ratio of vorticity associated with negative to positive initial vorticity, defined by equation (6), shown as a function of the ratio of final to initial depths (H/H_0) and the magnitude of initial vorticity normalized by f. The positive values (dotted lines) imply that no negative vorticity develops.

asymmetry. For example, $\omega_0/f \sim 5$ and $H/H_0 \sim 5$ for eddy A, yielding approximately a ratio of $-2/3$ and a ω/f of 30. Accordingly, the stretching of the planetary-vorticity tube may explain a part of the asymmetry shown in section 4.4.

[44] It should be noted that if vortex tubes return to their original generation sites on the coastal boundary (or other sites with the original depth), the above asymmetry caused by f would vanish. In the model results, however, virtually all eddies propagate away from the generation site (or shallow area adjacent to islands) and do not return (e.g., Figures 6 and 7) because of eddy dynamics, mean flow, and Stokes drift.

4.5.3. Advection by the Rotating Tidal Flow

[45] Although the above argument considers the case in which the magnitudes of depth change and initial vorticity are symmetric, a difference in these properties between CW and CCW eddies would augment (or diminish) asymmetric eddy formation. Here, we discuss the implication of differences in depth change, which can be caused by rotation in the tidal flow direction.

[46] The subinertial tidal flow over the sills in the straits rotates in a clockwise direction. (Note that this is attributed to the effects of topographically trapped waves [e.g., *Brink*, 1989; *Chapman*, 1989; NA00; *Ono et al.*, 2006] and hence occurs independently of the eddy generation discussed so far.) Accordingly, CCW eddies, which are generated on the left side of the strait facing downstream, are advected away from the coast toward the central part of the strait, leading to growth due to stretching (e.g., eddy A in Figure 6). In contrast, CW eddies, which are generated on the right side of the strait, are pushed toward the coast (e.g., Figure 8b), and therefore the stretching effect tends to be smaller for CW eddies than for CCW eddies. Further, the CW eddies advected toward the coast suffer stronger damping by bottom friction owing to shallower depths and by lateral friction.

[47] In extreme cases, the CCW eddy produced on the left side moves to the right side of the strait and seems to prevent the production of a CW eddy (e.g., eddy A in Figure 6d). The situation is similar to asymmetric eddy generation related to the initial conditions as seen in *Signell and Geyer* [1991]. However, in the case of the Kuril Straits, the asymmetry is created by the rotation of the tidal flow direction rather than through an arbitrary choice of the initial conditions.

4.6. Timescales of Eddy Propagation and Rotation

[48] The simulated eddies have another interesting property. The frequency of velocity fluctuations associated with eddies (observed at a fixed point) is significantly different from the tidal frequency. Figure 12 shows the temporal evolution of current velocity to the northeast of Simushir Island (near Ketoy Island) where eddy A passes (Figure 6). In Figure 12, disturbances with a timescale of approximately 4 hours are dominant and take place once per tidal cycle. These are associated with the passage of the CCW eddy A and the corresponding eddies generated in other tidal cycles. Since the southern portions of CCW eddies pass this site, the u component becomes positive while the v component first

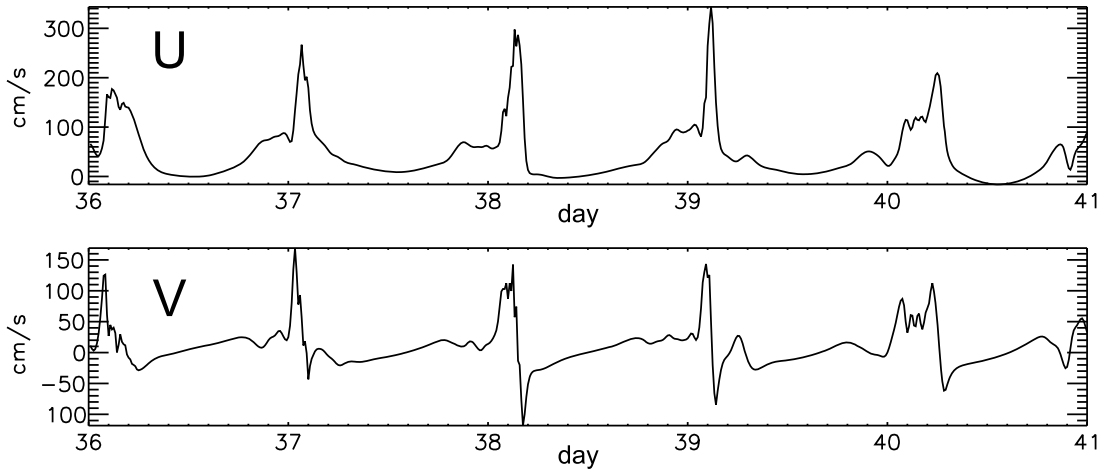

Figure 12. Temporal changes of u and v near the Okhotsk side of Ketoy Island, next to Simushir Island (x = 888 km, y = 340 km in Figure 6).

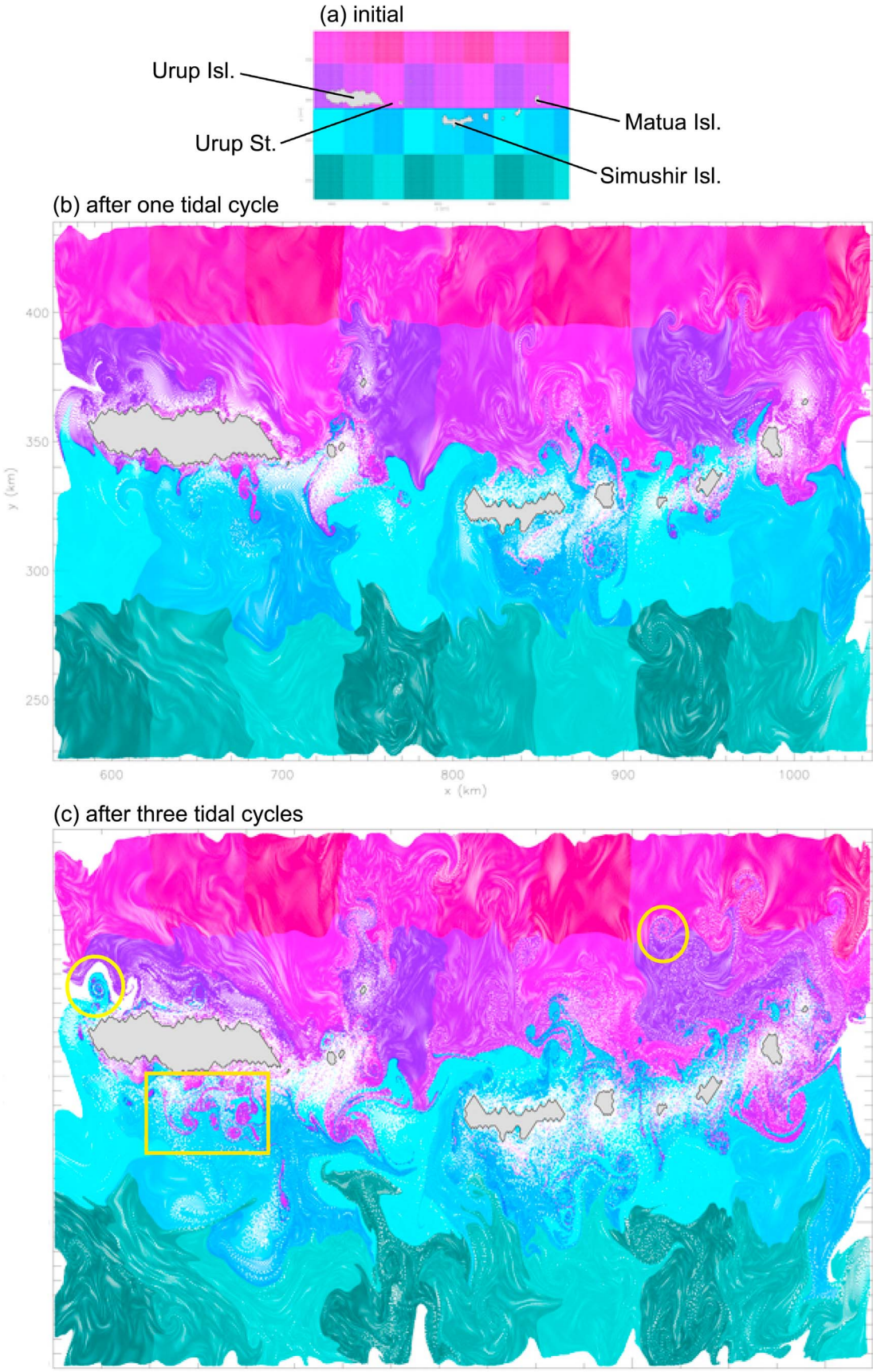

Figure 13. Results of particle tracking. Particle distributions (a) at the initial and after (b) one tidal cycle and (c) three tidal cycles.

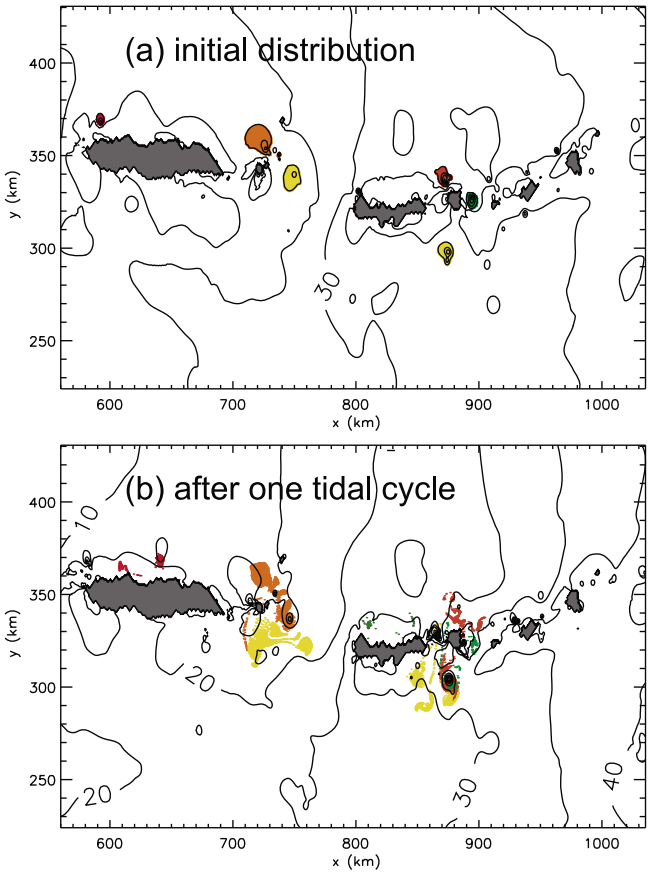

Figure 14. Results of particle tracking which are initially located in strong eddies. The distributions (a) at the initial and (b) after one tidal cycle.

takes negative and then subsequently assumes positive values. The above timescale yields a translation speed of 0.7 m s^{-1} using a diameter of 10 km. This estimate is similar to the translation speeds derived from Figure 6 (0.8 m s^{-1}).

[49] The fact that the above timescale of the eddies is significantly less than the tidal period indicates that the generation of these small-scale eddies induce energy transfer to higher frequencies. Accordingly, eddy generation could be a significant means of tidal energy dissipation (i.e., energy at the corresponding tidal frequency) in the Kuril Straits.

[50] In addition to the above timescale of propagation, eddies also have a timescale related to their rotation (i.e., the time that a water parcel takes to circulate around an eddy). As an example, the rotation timescale of eddy A may be estimated as 3 hours from $2\pi r/v_a$. Rotation timescales are estimated to be 2–30 hours. These values differ significantly from the tidal period, and hence it also supports the view that eddy generation dissipates a tidal energy. Also, the rotation timescale is similar to the propagation timescale for eddy A, and hence some water particles can be kept in the eddy and transported for a long distance while others flow into or out of the eddy, leading to mixing [e.g., *Flierl*, 1981].

4.7. Mixing and Transport

[51] Water movement associated with eddies is investigated by particle tracking, because the Lagrangian movement of water will differ greatly from the time-averaged Eulerian flow when such strong spatial variations are present [e.g., *Awaji et al.*, 1980]. Four particles are initially placed into each grid cell and are advected by the calculated velocity field. The results are shown in Figure 13. The particle distributions after both one tidal cycle and three tidal cycles clearly exhibit small scale features associated with eddies, although on the larger scale, particles tend to circulate around islands and/or sills with the shallower area on the right, which is consistent with the mean flow (Figure 4).

[52] Many small scale eddies are seen not only between Simushir and Matua Islands, but also around the Urup Strait and in the offshore regions. In these latter areas, most eddies do not produce large SSH anomalies, even though they are now clearly seen in Figure 13. In particular, regions to the south of Urup Island (where ten or more eddies are seen after three cycles) and to the west of Simushir Island (where some small eddies are seen after three cycles) represent areas where the satellite observations (Figures 2e and 2a, respectively) revealed small-scale eddies. Note that eddies near the straits become less apparent after three cycles since water near the straits is already well mixed at this time, while in the offshore regions where currents are weaker, eddies are more clearly seen after three cycles. (This is one reason why it is more difficult to detect small-scale eddies in TIR imagery in the northeastern part of the Kuril Islands.)

[53] The circulational features associated with eddies consist of roughly two types. Eddies of the first type exhibit spiral structures that entrain the ambient water particles (distinguished by different colors) into the eddies (e.g., those marked by circles in Figure 13c). This process is favorable for horizontal mixing. Eddies of the other type appear as small patches of water with a different color from that of the ambient water; The colors indicate that the initial positions of the water parcels differ from that of the ambient water, as is evident to the south of Urup Island (marked by a square in Figure 13c). Eddies of this type transport water away from the generation sites by trapping it inside their circulation system. (Note that the distinction between advection and mixing depends on the scales under consideration. Here, scales sufficiently larger than eddies are regarded as transport, whereas scales smaller than eddies are regarded as mixing.)

[54] To illustrate this process, the distribution of particles initially located in strong eddies (with SSH anomaly exceeding 10 cm, which corresponds to the eddy definition in section 4.4) after one tidal cycle is shown in Figure 14. Some eddies propagate but leave most of the water behind thereby, enhancing horizontal mixing (e.g., to the north of the Urup Strait and around Simushir Island), while others transport significant volumes of water trapped in their interior (e.g., to the north of Urup Island). Such features are qualitatively consistent with the expectations from the comparison of rotation and propagation timescales made in the previous subsection.

[55] To quantify the effect on mixing, we estimated the magnitude of stirring in terms of the temporal change in the variance of particle spread Φ, which is related to apparent diffusivity K by [*Awaji*, 1982]

$$K = \frac{1}{2}\frac{d\Phi}{dt} \simeq \frac{\Phi(T) - \Phi(0)}{2T},$$

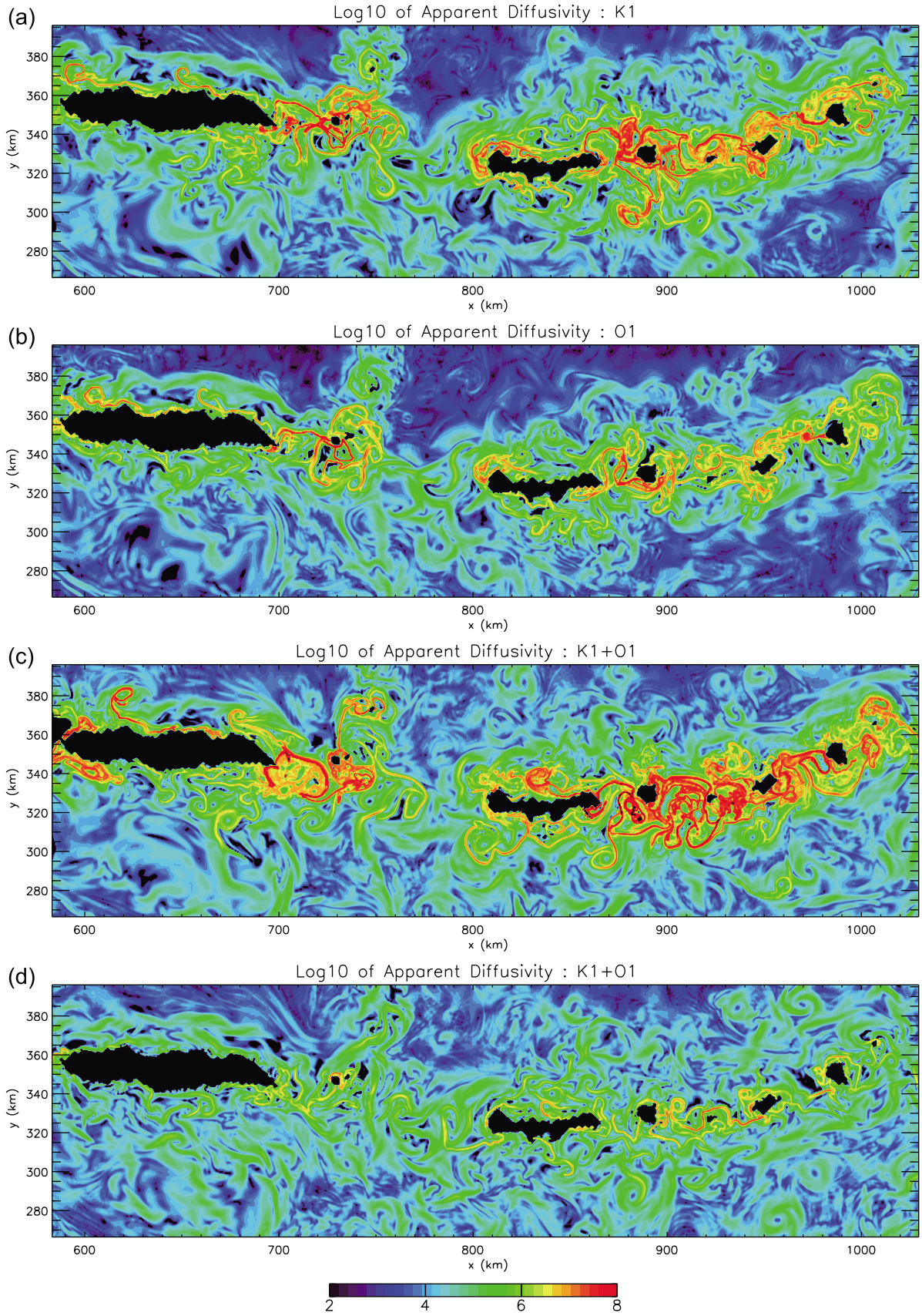

Figure 15. Distribution of apparent diffusivity ($cm^2\ s^{-1}$) for (a) K_1 and (b) O_1 cases and (c) the 'spring' and (d) 'neap' tides in the $K_1 + O_1$ case. The scale is logarithmic (base 10).

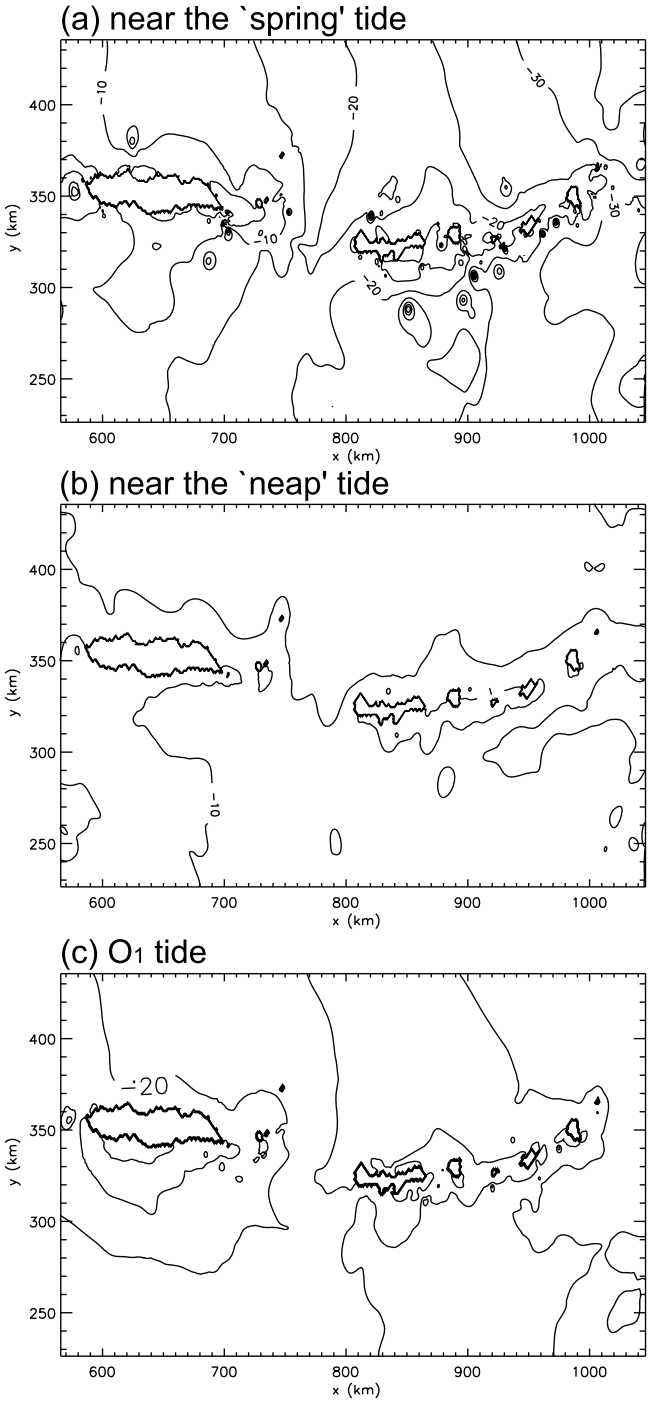

Figure 16. Sea surface height for the nearly diurnal period including (a) the 'spring' tide and (b) the 'neap' tide, respectively, and that for (c) the O_1 tide, at the time when the tidal currents turned to the $-x$ direction so that eddy growth nearly finished. This tidal phase corresponds to that of the K_1 case shown in Figure 5. Contour interval is 5 cm.

Here, Φ is calculated at each grid using 16 particles initially located in an area of 2 × 2 grids (∼1.1 km square), which sets the scale for K. The estimated apparent diffusivity is shown in Figure 15a. This quantity represents the eddy stirring effect rather well; the values are high particularly along tracks (and peripheries) of strong eddies, although this quantity includes stirring effects by both eddies and other currents (tidal currents, waves, and mean flow). The maximum value almost reaches 10^8 cm^2 s^{-1}, and similar values are distributed near the northeastern straits and the Urup Strait. The apparent diffusivity decreases rapidly away from the Island Chain, though stirring by eddies that propagate away from islands are still visible.

5. Modulation Due to the K_1 and O_1 Tides

[56] Thus far, we have investigated eddies generated by the K_1 tide alone (the K_1 case). Although the simulated eddies have similarities to those observed, the generation of eddies will depend on the speed of the tidal flow. We thus briefly discuss the effects of the tidal modulation on eddy generation, by comparing the $K_1 + O_1$ case with the K_1 and O_1 cases. The addition of the K_1 and O_1 tides results in amplitude modulation, which roughly corresponds to the springs-neaps cycle around this area, and whose carrier wave has a nearly diurnal period. (Hereafter, we use the terms, spring and neap tides, as an approximation.)

[57] The difference in the generation of strong eddies can be seen in Figure 16, which shows maps of SSH when the tidal currents are directed to the negative x direction (i.e., nearly along the island chain) so that eddies generated in the half period are well developed. During the nearly diurnal period corresponding to springs, strong eddies are generated in almost all the straits seen in the figure (Figure 16a). The number of strong eddies generated during this period is about 23 to 26 (here, a strong eddy is defined as an eddy whose SSH anomaly exceeds 10 cm, as discussed in section 4.4). This number is nearly twice that of the K_1 case alone (about 12 to 17) and more than twice that of the O_1 case alone (about 9 to 10). In contrast, only one or two strong-eddies are generated during the nearly diurnal period corresponding to neaps (Figure 16b).

[58] The strength of the eddies also differs greatly. Sea surface height anomalies associated with eddies that are generated during the nearly diurnal 'spring' tide (Figure 16a) are much larger than those associated with eddies generated during the 'neap' tide (Figure 16b). The former exceeds 60 cm at the maximum, whereas the latter is less than 15 cm at most. Furthermore, eddies generated by the K_1 tide are much stronger than those generated by the O_1 tide. The maximum surface displacement associated with eddies in the O_1 case is at most 25 cm, less than half that of the K_1 case.

[59] In this way, the number and the strength of the generated eddies are deeply affected by the modulation associated with the K_1 and O_1 tides. This suggests strong dependence on tidal flow speed and hence on tidal modulation. Associated with the change in eddy generation, the mixing induced by eddies also changes (Figures 15c and 15d).

6. Summary and Discussion

[60] We have shown the presence of eddies with diameters of a few kilometers to nearly 30 km around the Kuril Island Chain in high spatial resolution thermal infrared imagery derived by the LANDSAT mission. The horizontal scales of these eddies are much smaller than those of eddies discussed in previous studies (several tens of kilometers to some hundreds of kilometers).

[61] In order to gain an insight into the generation mechanism of such small-scale eddies, three barotropic tidal simulations were conducted in which K_1 and O_1 tides were calculated separately and simultaneously with a resolution of approximately 560 m. (The K_1 and O_1 tides represent the largest and the second largest constituents respectively in current speed around the Kuril Straits.)

[62] The K_1 tidal simulation produced numerous small-scale eddies in the northeastern part of the Kuril Island Chain and around Urup Island. The simulated eddies are similar to those observed in terms of horizontal scale, generation sites, and direction of rotation.

[63] The generation process of the simulated eddies has three characteristic features: (1) the generation occurs adjacent to islands on the downstream side of straits. (2) The eddies grow even after they leave the islands. (3) Counterclockwise (CCW) eddies generated on the left of the straits facing downstream are stronger and larger than clockwise (CW) eddies generated on the right.

[64] The first of these features is typical of the so-called headland eddies, which are generated through the effects of side boundaries, such as the vorticity supply from side boundaries and/or coastal geometry. The second feature is mainly caused by vorticity generation through the stretching term associated with relative vorticity. This term generates vorticity of the same sign as the eddy moves over the downstream side of sill to the deeper water.

[65] The third feature, the asymmetry, is quantified by eddy statistics. CCW eddies tend to be larger in number and size and stronger in vorticity and surface displacement in the parameter regime of the cyclostrophic wind balance as well as the gradient wind balance regime. The asymmetry of similar magnitudes can be caused by the stretching of planetary vorticity tubes and the clockwise rotation of the tidal flow direction even in the regime of the cyclostrophic wind balance. The simple estimate presented in section 4.5.2 shows that the effect of the planetary vorticity stretching term can make eddy growth significantly asymmetric even in a parameter range where relative vorticity of an eddy becomes much greater than the planetary vorticity after the growth. In addition, as the tidal flow rotates clockwise in the straits, the advection moves CCW eddies offshore (left to right facing downstream) and CW eddies onshore. This makes vorticity-tube stretching stronger for CCW eddies. In addition, as CW eddies stay close to the coast, high bottom friction in shallow water, lateral friction at the coast, and/or the CCW eddy that is advected from the opposite side of the strait tend to weaken the CW eddies, leading to asymmetry in eddy strength.

[66] Some of the eddies move offshore and thus affect water mixing and transport in both near and offshore regions of the straits, as our results of particle tracking using the simulated current field show. Strong mixing is induced particularly along tracks of strong eddies in the vicinity of straits and islands, resulting in apparent diffusivity of nearly 10^8 cm^2s^{-1}. In addition, the generation of small-scale eddies acts as a tidal-energy dissipation mechanism, because the timescales of velocity fluctuations (observed at a fixed point) associated with the simulated eddies are of the order of hours, significantly shorter than the tidal period.

[67] The eddy generation is strongly affected by the modulation due to the K_1 and O_1 tides. The number of strong eddies generated roughly doubles during the diurnal period associated with the springs relative to the K_1 case alone and becomes almost zero during neaps periods. Eddy strength (e.g., associated SSH anomaly or relative vorticity) and induced mixing also vary greatly throughout the springs-neaps cycle.

[68] The above barotropic tidal simulations have revealed a likely generation mechanism, the asymmetry in main properties, and mixing effect of small-scale eddies around the Kuril Straits, in addition to the influence of tidal modulation. Nevertheless, because simulation results have limitations due to the resolution and accuracy of topographic data, in situ measurements are desired in the future to confirm the eddy generation mechanism and causes of asymmetry. Also, quantitative estimates of the effects of the eddies and tidal modulation need to be improved by taking into consideration the effects of stratification and other currents such as wind-driven circulation, the effects of other tidal constituents, and so on. In addition, the qualitative generation mechanism suggested here may be improved in a more quantitative analysis that includes explicitly the effects of nonlinearity due to eddy-induced flow and finite eddy size, for example. Moreover, quantitative observational estimates of eddy properties would be desired based on a broader satellite-image database. These aspects are beyond the scope of this study and are left for future work.

[69] **Acknowledgments.** We appreciate Y. Kanno for his help in conducting the model integrations and preliminary analysis and G. Mizuta, N. Ebuchi, T. Horinouchi, and K. Ohshima for their useful comments. Thanks are extended to anonymous reviewers for their useful comments. T.N. was partly supported by a JSPS Research Fellowship for Young Scientists. T.A. was partly supported by the Category 7 of MEXT RR2002 Project for Sustainable Coexistence of Human, Nature and the Earth and by a Grant-in-Aid for the 21st Century COE Program (Kyoto University, G3). Numerical calculations were done on the VPP800 at the Data Processing Center of Kyoto University and on the PORC information system at ILTS Hokkaido University.

References

Awaji, T. (1982), Water mixing in a tidal current and the effect of turbulence on tidal exchange through a strait, *J. Phys. Oceanogr.*, *12*, 501–514.

Awaji, T., N. Imasato, and K. Kunishi (1980), Tidal exchange through a strait: A numerical experiment using a simple model basin, *J. Phys. Oceanogr.*, *10*, 1499–1508.

Brink, K. H. (1989), The effect of stratification on seamount-trapped waves, *Deep Sea Res., Part A*, *36*, 825–844.

Chapman, D. C. (1989), Enhanced subinertial diurnal tides over isolated topographic features, *Deep Sea Res., Part A*, *36*, 815–824.

Dong, C., J. C. McWilliams, and A. F. Shchepetkin (2007), Island wakes in deep water, *J. Phys. Oceanogr.*, *37*, 962–981.

Eldevik, T., and K. B. Dysthe (2002), Spiral eddies, *J. Phys. Oceanogr.*, *32*, 851–869.

Flierl, G. R. (1981), Particle motions in large amplitude wave fields, *Geophys. Astrophys. Fluid Dyn.*, *18*, 39–74.

Holton, J. R. (1992), *An Introduction to Dynamic Meteorology*, 3rd ed., Academic, San Diego, Calif.

Huthnance, J. M. (1981), On mass transports generated by tides and long waves, *J. Fluid Mech.*, *102*, 367–387.

Isern-Fontanet, J., E. Gracía-Ladona, and J. Font (2006), Vortices of the Mediterranean Sea: An altimetric perspective, *J. Phys. Oceanogr.*, *36*, 87–103.

Kantha, L. H. (1995), Barotropic tides in the global oceans from a nonlinear tidal model assimilating altimetric tides: 1. Model description and results, *J. Geophys. Res.*, *100*, 25,283–25,308.

Kitani, K. (1973), An oceanographic study of the Okhotsk Sea: Particularly in regard to cold waters, *Bull. Far Seas Fish. Res. Lab.*, *9*, 45–77.

Klinger, B. A. (1994), Inviscid current separation from rounded capes, *J. Phys. Oceanogr.*, *24*, 1805–1811.

Kloosterziel, R. C., and G. J. F. Van Heijst (1991), An experimental study of unstable barotropic vortices in a rotating fluid, *J. Fluid Mech.*, *223*, 1–24.

Kowalik, Z., and I. Polyakov (1998), Tides in the Sea of Okhotsk, *J. Phys. Oceanogr.*, *28*, 1389–1409.

LaCasce, J. H., O. A. Nost, and P. E. Isachsen (2008), Asymmetry of free circulations in closed ocean gyres, *J. Phys. Oceanogr.*, *38*(2), 517–526.

Lee, S.-H., and K. Kim (1999), Scattering of tidal frequency waves around a cylindrical island, *J. Phys. Oceanogr.*, *29*, 436–448.

Matsumoto, K., T. Takanezawa, and M. Ooe (2000), Ocean tide models developed by assimilating TOPEX/POSEIDON altimeter data into hydrodynamical model: A global model and regional model around Japan, *J. Oceanogr.*, *56*, 567–581.

Moisy, F., C. Morize, M. Rabaud, and J. Sommeria (2011), Decay laws, anisotropy and cyclone-anticyclone asymmetry in decaying rotating turbulence, *J. Fluid Mech*, *666*, 5–35.

Nakamura, T., and T. Awaji (2004), Tidally-induced diapycnal mixing in the Kuril Straits and its role in water transformation and transport: A three dimensional nonhydrostatic model experiment, *J. Geophys. Res.*, *109*, C09S07, doi:10.1029/2003JC001850.

Nakamura, T., T. Awaji, T. Hatayama, K. Akitomo, T. Takizawa, T. Kono, Y. Kawasaki, and M. Fukasawa (2000a), The generation of large-amplitude unsteady lee waves by subinertial K_1 tidal flow: A possible vertical mixing mechanism in the Kuril Straits, *J. Phys. Oceanogr.*, *30*, 1601–1621.

Nakamura, T., T. Awaji, T. Hatayama, K. Akitomo, and T. Takizawa (2000b), Tidal exchange through the Kuril Straits, *J. Phys. Oceanogr.*, *30*, 1622–1644.

Nakamura, T., T. Awaji, T. Toyoda, and Y. Ishikawa (2003), Coastal Oyashio in a North Pacific simulation experiment [in Japanese with English abstract], *Bull. Coastal Oceanogr.*, *41*(1), 13–22.

Nakamura T., T. Toyoda, Y. Ishikawa, and T. Awaji (2004), Tidal mixing in the Kuril Straits and its impact on ventilation in the North Pacific Ocean, *J. Oceanogr.*, *60*, 411–423.

Nakamura T., T. Toyoda, Y. Ishikawa, and T. Awaji (2006a), Enhanced ventilation in the Okhotsk Sea through tidal mixing at the Kuril Straits, *Deep Sea Res., Part I*, *53*, 425–448.

Nakamura T., T. Toyoda, Y. Ishikawa, and T. Awaji (2006b), Effects of tidal mixing at the Kuril Straits on the North Pacific ventilation: Adjustment of intermediate layers revealed from numerical experiments, *J. Geophys. Res.*, *111*, C04003, doi:10.1029/2005JC003142.

National Geophysical Data Center (1988), ETOPO5: Digital relief of the surface of the Earth, *Data Announce. 88-MGG-02*, Natl. Geophys. Data Cent., NOAA, Boulder, Colo.

Nøst, O. A., J. Nilsson, and J. Nycander (2008), On the asymmetry between cyclonic and anticyclonic flow in basins with sloping boundaries, *J. Phys. Oceanogr.*, *38*, 771–787.

Ohshima, K. I. (2005), A generation mechanism for mesoscale eddies in the Kuril Basin of the Okhotsk Sea: Baroclinic instability caused by enhanced tidal mixing, *J. Oceanogr.*, *61*, 247–260.

Okubo (1970), Horizontal dispersion of floatable particles in the vicinity of velocity singularities such as convergences, *Deep Sea Res. Oceanogr. Abstr.*, *17*, 445–454.

Ono, J., K. I. Ohshima, G. Mizuta, Y. Fukamachi, and M. Wakatsuchi (2006), Amplification of diurnal tides over Kashevarov Bank in the Sea of Okhotsk and its impact on water mixing and sea ice, *Deep Sea Res., Part I*, *53*, 409–424.

Ooyama, K. (1966), On the stability of the baroclinic circular vortex: A sufficient criterion for instability, *J. Atmos. Sci.*, *23*, 43–53.

Orlanski, I. (1976), A simple boundary condition for unbounded hyperbolic flows, *J. Comput. Phys.*, *21*, 251–269.

Polvani, L. M., J. C. McWilliams, M. A. Spall, and R. Ford (1994), The coherent structures of shallow water turbulence: Deformation radius effects, cyclone/anticyclone asymmetry and gravity wave formation, *Chaos*, *4*, 177–186.

Rabinovich, A. B., and R. E. Thomson (2001), Evidence of diurnal shelf waves in satellite-tracked drifter trajectories off the Kuril Island, *J. Phys. Oceanogr.*, *31*, 2650–2668.

Ray, R. D. (1999), A global ocean tide model from TOPEX/POSEIDON altimetry: GOT99.2, *NASA Tech. Memo., 209478*, Goddard Space Flight Cent., Greenbelt, Md.

Robinson, I. S. (1981), Tidal vorticity and residual circulation, *Deep Sea Res., Part A*, *28*, 195–212.

Schwiderski, E. W. (1980), On charting global ocean tides, *Rev. Geophys.*, *18*, 243–268.

Signell, R. P., and W. R. Geyer (1991), Transient eddy formation around headlands, *J. Geophys. Res.*, *96*, 2561–2575.

Smith, W. H. F., and D. T. Sandwell (1997), Global sea floor topography from satellite altimetry and ship depth soundings, *Science*, *277*, 1956–1962.

Talley, L. D. (1991), An Okhotsk Sea water anomaly: Implications for ventilation in the North Pacific, *Deep Sea Res., Part A*, *38*, S171–S190.

Talley, L. D. (1993), Distribution and formation of North Pacific Intermediate Water, *J. Phys. Oceanogr.*, *23*, 517–537.

Uchimoto, K., H. Mitsudera, and N. Ebuchi (2007), Anticyclonic eddy caused by the soya warm current in an Okhotsk OGCM, *J. Oceanogr.*, *63*, 379–391.

Wakatsuchi, M., and S. Martin (1991), Water circulation of the Kuril Basin of the Okhotsk Sea and its relation to eddy formation, *J. Oceanogr. Soc. Jpn.*, *47*, 152–168.

Watanabe, T., and M. Wakatsuchi (1998), Formation of 26.8 σ_θ water in the Kuril Basin of the Sea of Okhotsk as a possible origin of North Pacific Intermediate Water, *J. Geophys. Res.*, *103*, 2849–2865.

Weiss, J. (1991), The dynamics of enstrophy transfer in two-dimensional hydrodynamics, *Phys. D*, *48*, 273–294, doi:10.1016/0167-2789(91)90088-Q.

Yasuda, I. (1997), The origin of the North Pacific intermediate water, *J. Geophys. Res.*, *102*, 893–910.

Yasuda, I., et al. (2000), Cold-core anticyclonic eddies south of the Bussol' Strait in the northwestern subarctic Pacific, *J. Phys. Oceanogr.*, *30*, 1137–1157.